chemistry

MDPI

Article

How Topological Differences between Two Oxide Surfaces Determine Selectivity—The Case of the Dehydra-Decyclization of Tetrahydrofuran

Sai Praneet Batchu [1,2], Stavros Caratzoulas [2] and Dionisios G. Vlachos [1,2,*]

[1] Department of Chemical and Biomolecular Engineering, University of Delaware, Newark, DE 19716, USA
[2] Catalysis Center for Energy Innovation, University of Delaware, Newark, DE 19716, USA
* Correspondence: vlachos@udel.edu

Abstract: Production of butadiene from biomass-based tetrahydrofuran (THF) is explored as an alternative to the existing petroleum-based processes. Metal oxide catalysts have been shown to exhibit varying product selectivities when reacted with THF. Among those oxides, ZrO_2 showed the highest selectivity for butadiene. In contrast, Al_2O_3 showed the highest selectivity for the competing retro-Prins products, C_3H_6 and HCHO. The reasons behind the varying selectivity across oxides are unclear. In this work, we employ periodic density functional theory and mean-field microkinetic modeling to investigate the mechanism of the reaction of THF to butadiene and retro-Prins products on t-ZrO_2 (101) (dry and hydrous) and on γ-Al_2O_3 (110). Our simulations reproduce the experimental selectivity trends. High selectivity for butadiene is promoted by the presence of neighboring Lewis acid metal sites that facilitate E1cB hydroxyl elimination from a 3-butenoxide intermediate; on hydrous Al_2O_3; where such neighboring Lewis acid centers are not available, the butenoxide undergoes E2 elimination and retro-Prins products ensue. The THF ring opening is rate-determining on ZrO_2, whereas the γ-proton elimination that yields the 3-butenoxide intermediate is rate controlling on hydroxylated Al_2O_3. We conclude that the local topology around the active site greatly influences the mechanism and selectivity.

Keywords: biomass; butadiene; tetrahydrofuran; metal oxide; density functional theory; microkinetic modelling; ZrO_2; Al_2O_3

check for updates

Citation: Batchu, S.P.; Caratzoulas, S.; Vlachos, D.G. How Topological Differences between Two Oxide Surfaces Determine Selectivity—The Case of the Dehydra-Decyclization of Tetrahydrofuran. *Chemistry* **2023**, *5*, 422–437. https://doi.org/10.3390/chemistry5010031

Academic Editors: José Antonio Odriozola and Hermenegildo García

Received: 31 January 2023
Revised: 26 February 2023
Accepted: 27 February 2023
Published: 1 March 2023

Copyright: © 2023 by the authors. Licensee MDPI, Basel, Switzerland. This article is an open access article distributed under the terms and conditions of the Creative Commons Attribution (CC BY) license (https://creativecommons.org/licenses/by/4.0/).

1. Introduction

1,3-Butadiene is an important, high-demand chemical used in the manufacture of styrene-butadiene rubber (SBR) and acrylonitrile-butadiene-styrene (ABS). Currently, butadiene and other C4 compounds are produced as side products in the production of ethylene by steam cracking of crude oil. However, the current revolution in shale gas (primarily light hydrocarbons) is resulting in diminished butadiene production, thereby increasing its demand-supply gap. Moreover, non-renewable feedstocks, high reaction temperatures and high C4 separation costs involved in the existing technologies further exacerbate the situation. Thus, it is highly desirable to establish greener alternative processes for 'on-purpose' butadiene production. Biomass-based butadiene production is a potential alternative as it involves renewable feedstocks and catalytic reactions typically run at lower temperatures than steam cracking.

Dehydra-decyclization of biomass-derived tetrahydrofuran (THF) [1–4] is a promising route to butadiene. The reaction can be catalyzed by Brønsted acid catalysts [5–7], and mechanistic studies on H-[Al]MFI [8] have elucidated the mechanism. However, Brønsted acids also catalyze the retro-Prins condensation to propene and formaldehyde [8], the major side reaction (ca. 30% selectivity at 220–270 °C) that suppresses the formation of butadiene. On H-[Al]MFI [8], dehydra-decyclization to butadiene (Scheme 1) proceeds through 2-buten-1-ol, which forms by 1,2-hydride shift in the primary 4-hydroxybutyl

oxide intermediate that forms from the THF ring opening; the 2-buten-1-ol subsequently undergoes Brønsted-catalyzed E2 elimination to the diene [8]. If the protonated open ring (primary 4-hydroxyl butyl cation) is not effectively stabilized by the conjugate base, then it can undergo coordinated 1,2-hydride shift and C-C bond scission yielding propene and formaldehyde (Scheme 1). Although substantially less likely, this coordinated nuclear motion remains kinetically possible after the stabilization of the 4-hydroxyl butyl cation by the conjugate base [8]. These insights lend perspective to the work of Abdelrahman et al. [5] and Kumar et al. [7], who reported that P-SPP (phosphorus-self pillared pentasil) [5,9] and B-MWW (framework boron-containing MWW) are less selective than H-ZSM5 for retro-Prins products when reacted with THF, presumably on account of their weak Brønsted acidity. The lower selectivity for retro-Prins notwithstanding, the rate of butadiene formation over weak Brønsted acids is low.

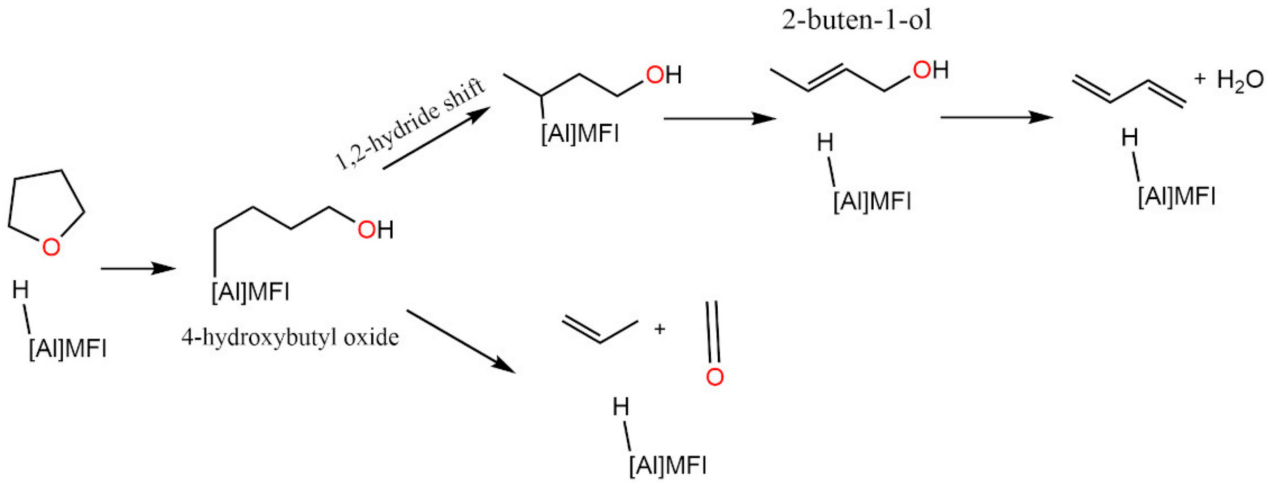

Scheme 1. Dominant reaction pathways for conversion of THF to butadiene and propene on H-[Al]MFI [8].

Venturing into the Lewis catalyst space, and after testing several metal oxide catalysts (ZrO_2, CeO_2, TiO_2, Nb_2O_5, WO_x/ZrO_2), Ji et al. [10] reported that ZrO_2 consistently exhibited the highest selectivity for 1,3-butadiene (ca. 90%) when reacted with THF. Its catalytic performance was also structure-insensitive and the catalyst was relatively stable with time on stream—although the tetragonal phase of ZrO_2 was found to be the most stable one. Apart from Al_2O_3, which was ca. 90% selective for retro-Prins products, the rest of the oxides were more selective than H-ZSM5 for 1,3-butadiene. Adding to its high selectivity for dienes, ZrO_2 is also highly selective for a single diene isomer when multiple dienes can form (C5+) [11].

In this work, we undertake mechanistic studies aimed at understanding the different performance of ZrO_2 and Al_2O_3 when reacted with THF. We perform periodic density-functional theory (DFT) calculations and microkinetic simulations to investigate the reaction mechanisms of the conversion of THF to butadiene and retro-Prins products on the models of the predominant facets of t-ZrO_2 and γ-Al_2O_3 [10,12–14]. Although butanal can form and subsequently undergo hydrogenation to butene [10,15,16], this is not a reaction pathway we have investigated here, as Ji et al. reported only the presence of trace amounts of butene. The kinetic parameters and selectivity values obtained from the simulations are compared with available experimental data [10]. Last, we provide insights into the factors that bring about selectivity on ZrO_2 and Al_2O_3.

2. Materials and Methods

2.1. DFT Simulations

Periodic DFT calculations were performed using the Vienna ab-initio simulation package (VASP 5.4.1). The core electrons were modeled with the projector augmented

wavefunction (PAW) pseudopotential, and the valence electrons were modeled with the Perdew−Burke−Ernzerhof (PBE) exchange-correlation functional and a plane-wave basis set with energy cut-off at 400 eV [17,18]. Dispersion interactions were modeled using the D3 method of Grimme with Becky-Johnson dampening [19]. Transition states were determined using the nudged-elastic band (NEB) + dimer [20] or the NEB + climb [21] method. Electronic energies and ionic forces were converged to 10^{-6} eV and 0.02 eV/Å, respectively. For the very few transition state calculations that could not converge to 0.02 eV/Å, we relaxed the cut-off criterion to a higher value (up to 0.05 eV/Å). The ionic degrees of freedom were optimized using the conjugate gradient algorithm. Vibrational frequencies were estimated by partial diagonalization of the Hessian matrix using nuclear displacements of 0.015 Å. For shallow, first-order saddle points, a displacement of 0.002 Å was deemed necessary to eliminate redundant imaginary frequencies. Thermal corrections to the electronic energies at 673.15 K were calculated using the quasi-rigid-rotor-harmonic-oscillator (quasi-RRHO) model proposed by Grimme and Li et al. [22,23]; the vibrational enthalpies and entropies corresponding to modes below 100 cm^{-1} have been replaced by corresponding free-rotor values. Small imaginary frequencies appear in a few stationary and transition states, and they have been replaced by a wavenumber below 100 cm^{-1} (50 cm^{-1}) [24]. The energies of gas phase molecules were referenced to the corresponding experimental values obtained from NIST and RMG-MIT databases using the referencing scheme in pMuTT [25].

The (101) termination of tetragonal ZrO_2 (t-ZrO_2) was represented by a (2 × 4 × 1) periodic slab (dimensions 12.89 Å × 14.58 Å × 28.86 Å) (Figure 1a). The model consists of 4 Zr-O layers with the bottom two layers frozen and a vacuum spacing of 20 Å along the z-direction between the periodic images (Figure 1a,b). The reciprocal space was sampled on a 3 × 3 × 1 k-point mesh. The 4s, 4p, 4d, and 5s electrons of Zr were treated as valence electrons. Hubbard's U parameter with a U value of 4 eV [26] was added to the Hamiltonian to reduce the delocalization of the outermost d-electrons. This model consists of 64 Zr atoms and 128 O atoms. There are two types of surface Zr atoms (Zr_a and Zr_b) and two types of O atoms (O_{3a} and O_{3b}). The Zr in the bulk is coordinated to eight O atoms whereas the surface Zr atoms are hepta-coordinated to O atoms, three of them on the surface and the other four in the sub-surface layers. The bulk O atoms are coordinated to four Zr atoms whereas the surface O atoms are coordinated to three Zr atoms.

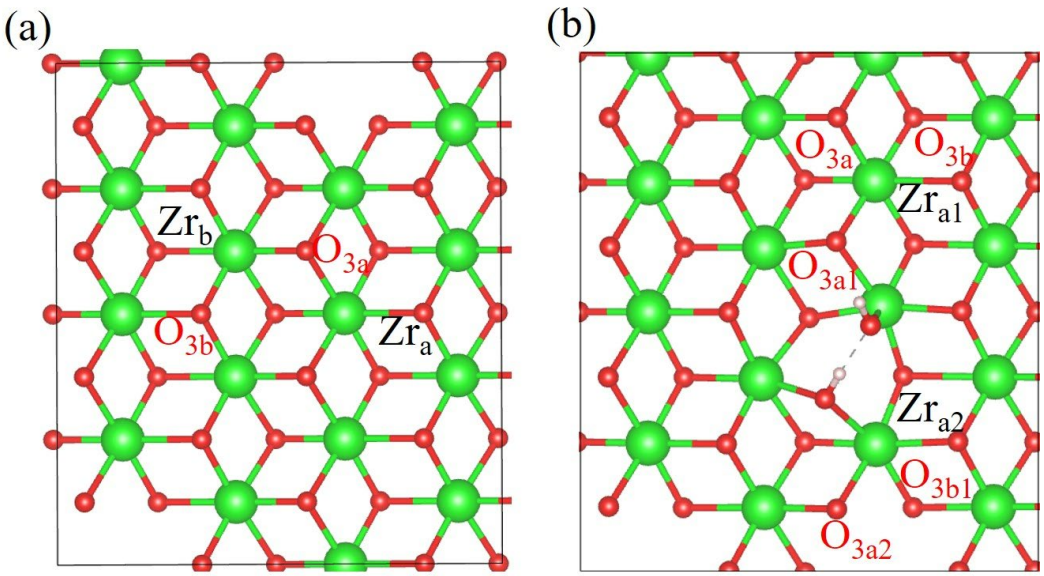

Figure 1. *Cont.*

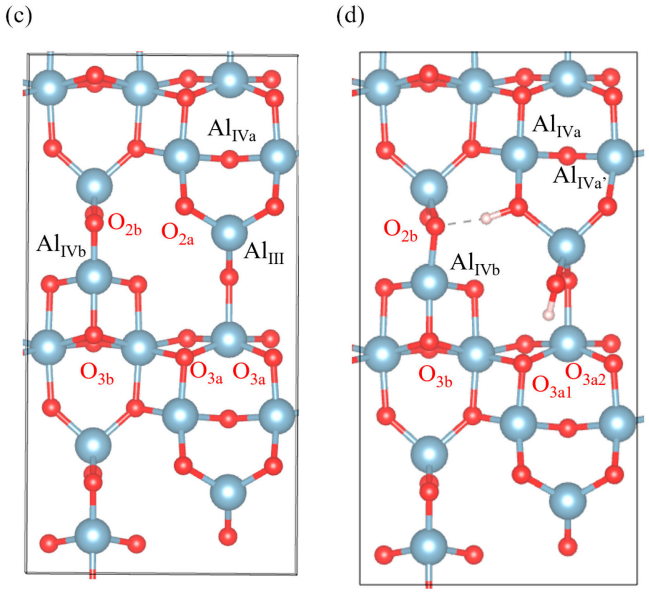

Figure 1. Top view of catalyst surface models of (**a**) dry t-ZrO_2 (101); (**b**) hydroxylated t-ZrO_2 (101); (**c**) dry γ-Al_2O_3 (110); and (**d**) hydroxylated γ-Al_2O_3 (110).

We model Al_2O_3 as a 2 × 1 unit cell (dimensions 8.40 Å × 16.14 Å × 27.40 Å) of (110) termination of γ-Al_2O_3 (Figure 1c) [12,27]. The model consists of 32 Al atoms and 48 O atoms. The bottom Al-O layer (8 Al and 12 O atoms) is frozen, and a vacuum spacing of 24 Å along the z-direction between the periodic images. The reciprocal space was sampled on a 3 × 2 × 1 k-point mesh. The 3s and 3p electrons of Al were treated as valence electrons. As shown in (Figure 1c), the surface consists of different types of under-coordinated Al and O sites. In the case of Al sites, there are tri-coordinated Al_{III} sites, and two types of tetra-coordinated Al sites, namely Al_{IVa} and Al_{IVb}. There are two types of di-coordinated O atoms (O_{2a} and O_{2b}) and two types of tri-coordinated O atoms (O_{3a} and O_{3b}). We model the hydroxylated surfaces of ZrO_2 (Figure 1b) and Al_2O_3 (Figure 1d) by chemisorbing a H_2O molecule on the most Lewis acid-base pairs, Zr_a-O_{3a} and Al_{III}-O_{2a} of ZrO_2 and Al_2O_3, respectively. The coordinate files of the ZrO_2 and Al_2O_3 models are provided in the Supplementary Materials.

2.2. Microkinetic Simulations

Microkinetic modeling was performed using CHEMKIN [28]. The simulations were run at a temperature of 673.15 K and total pressure of 1 atm. The mole fraction of THF in the feed is 0.05, with the rest being an inert gas, and these values are chosen based on the experiments performed by Ji et al. [10]. The PFR reactor was modeled as a series of 900 CSTR reactors. The values of the input parameters and details about evaluating them are provided in Section S1 in the Supplementary Materials. Sensitivity analysis was performed by perturbing the forward and backward rate constants by ±4%.

3. Results

3.1. Dry t-ZrO_2 (101)

The t-ZrO_2 (101) surface exposes two distinct Zr sites, denoted as Zr_a and Zr_b in Figure 1a. Surface-bound THF interacts with either of these two sites via its ring-O alone (ring in upright configuration) and the respective binding energies relative to gas-phase THF are −1.13 and −0.95 eV.

Pathway 1_Zrd in Scheme 2 depicts the dominant route to butadiene. Considering the salient elements of it (a detailed description is in Section S2.1 in the Supplementary Materials), we see that there is substantial departure from the mechanism on H-[Al]MFI outlined above—but there are also elements reminiscent of it. Following the ring opening,

the O atom of THF is coordinated by Lewis acidic surface Zr and the oxide stabilizes the primary carbocation ($\mathbf{2_{Zrd}}$) via coordination by a surface O. Intermediate $\mathbf{2_{Zrd}}$ then undergoes γ-proton elimination by a surface oxygen to form the 3-butenoxide intermediate ($\mathbf{3_{Zrd}}$). Butadiene ($\mathbf{5_{Zrd}}$) forms through the 2-butenoxide intermediate $\mathbf{4_{Zrd}}$, which is reminiscent of the 2-buten-1-ol intermediate on H-[Al]MFI. However, on the oxide, the double bond shift from $\mathbf{3_{Zrd}}$ to $\mathbf{4_{Zrd}}$ is effected by elimination of the allylic proton by a surface oxygen. The THF O atom, which has been coordinated to a surface Zr all the while, attracts one of the two surface protons in the vicinity, and this sets off the C-O bond breaking along with rehybridization of the backbone carbons yielding butadiene.

Pathway 2_Zrd in Scheme 3 is the kinetically dominant mechanism to retro-Prins products. It is remarkably similar to the mechanism on H-[Al]MFI as the stabilized primary carbocation $\mathbf{2_{Zrd}}$ undergoes coordinated 1,2-hydride shift from C4 to C5 and C2-C3 bond scission. The free energy and enthalpy profiles of all the pathways are shown in Figure S1. The adsorption of THF ($\Delta H_{ads} = -1.14$ eV), H_2O ($\Delta H_{ads} = -1.5$ eV), and HCHO ($\Delta H_{ads} = -0.63$ eV) is exothermic (Figure S1b). From the adsorption enthalpies, we can conclude that THF and HCHO chemisorb on the surface—by strongly interacting with the Lewis-acidic Zr sites via the lone pairs of the O atoms in these molecules. When compared to the rest of the reactant and product species, H_2O binds the strongest to the surface via dissociative chemisorption, and this strong binding of H_2O is also reflected in the highest free energy-based stability of the intermediate (6_{Zrd}) (Figure S1a).

For completeness, two more retro-Prins pathways (pathways 3_Zrd and 4_Zrd) and the corresponding free energy profiles are described in the Supplementary Materials (Section S2.1) but they do not contribute in any significant way as microkinetic analysis shows that 99.9% of the reactive flux is on the butadiene Pathway 1_Zrd while the remaining 0.1% of it is on the retro-Prins Pathway 2_Zrd (Table S5). The product selectivities are in satisfactory agreement with the experimental values (Figure S2) [10].

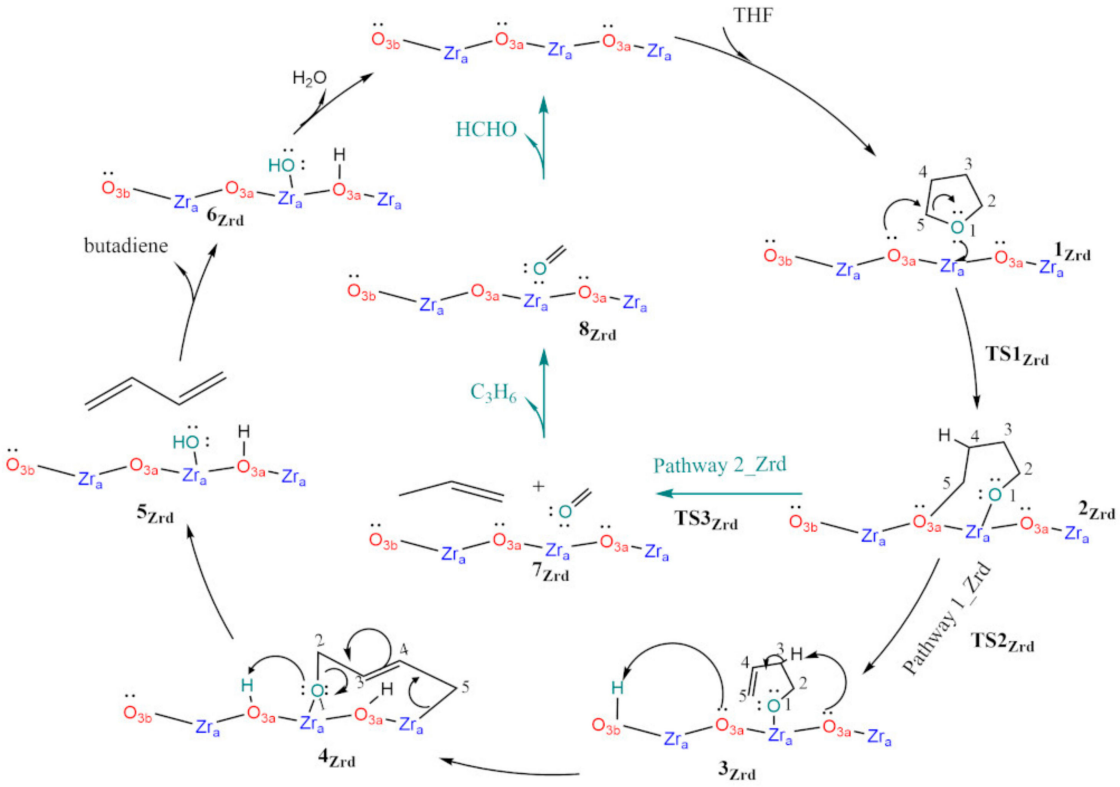

Scheme 2. THF reaction mechanism to butadiene and retro-Prins products on dry t-ZrO_2 (101). Pathway 1_Zrd (in black): butadiene; Pathway 2_Zrd (in green): retro-Prins products. ('Zrd' stands for dry ZrO_2).

Sensitivity analysis (Figure 2a,b) shows that the ring opening ($TS1_{Zrd}$) primarily and the γ-proton elimination ($TS2_{Zrd}$) to a lesser extent control the rate of butadiene formation. Since $S_{butadiene}$ is nearly 100%, the selectivity for butadiene is insensitive to any of the elementary steps. On the other hand, the rate and selectivity for propene are enhanced by $TS3_{Zrd}$ and the hydride-shift $TS4_{Zrd}$ (for $TS4_{Zrd}$, see Scheme S1 in Supplementary Materials) and hampered by the γ-H abstraction. Since the ring opening transition state ($TS1_{Zrd}$) is higher than all the rest and is common to all the pathways, it also enhances the rate for propene formation. Surface coverage analysis shows that the chemisorbed H_2O (**6_{Zrd}**) is the most abundant reaction intermediate on account of its stability (see profile in Figure S1); water coverage increases with conversion (Figure 2c).

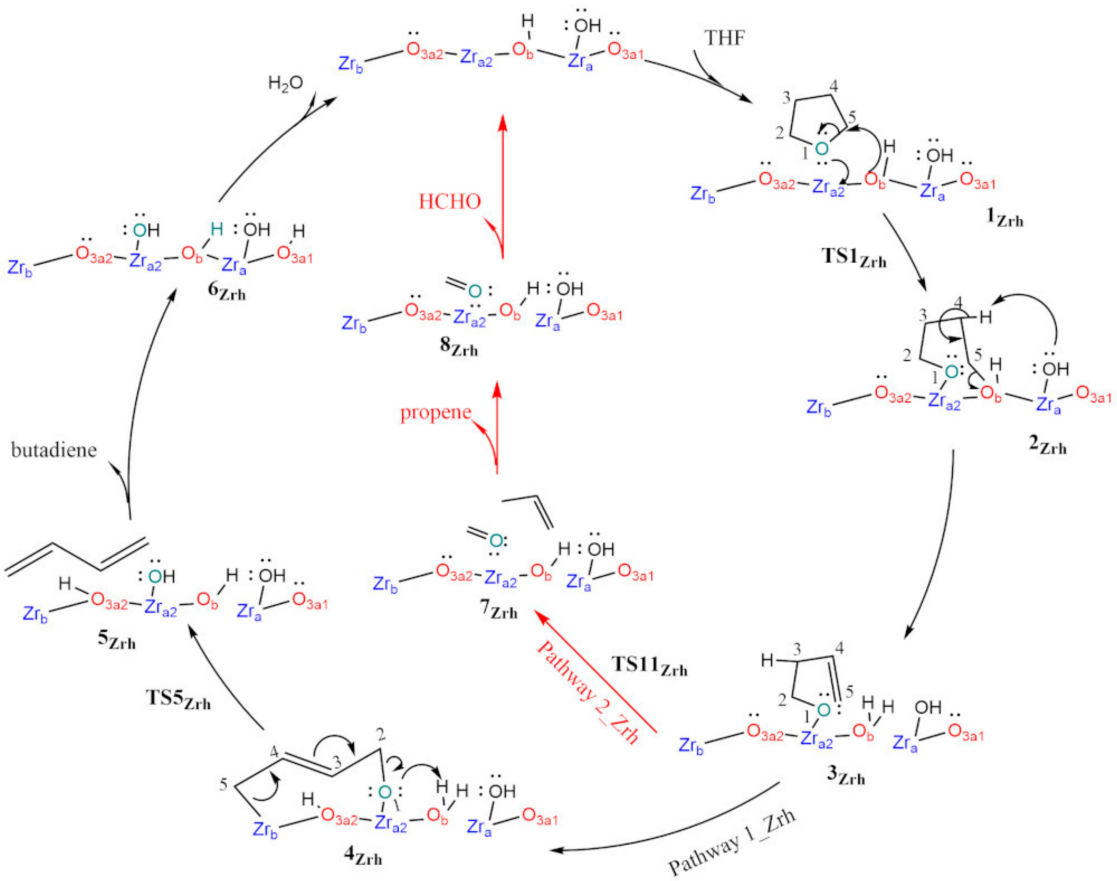

Scheme 3. Mechanism of THF reaction to butadiene and retro-Prins products on hydroxylated t-ZrO_2(101). Pathway 1_Zrh (in black): butadiene; Pathway 2_Zrh (in red): retro-Prins products. ('Zrh' stands for hydroxylated ZrO_2).

3.2. Hydroxylated t-ZrO_2 (101)

The hydroxylated t-ZrO_2 (101) model (Figure 1b) consists of chemisorbed H_2O on a Zr_a-O_{3a} pair, forming a terminal and a bridging OH group; this model corresponds to 1 H_2O molecule/supercell with the corresponding surface coverage being 8.82×10^{-10} mol/cm^2. To investigate the effect of the OH groups on the mechanism, we put THF on sites nearest to the OH groups, Zr_{a1} and Zr_{a2} sites. The THF binding energies on Zr_{a1} and Zr_{a2} are nearly the same, −1.06 and −1.05 eV, respectively. For the subsequent ring opening, we evaluate the free energy barriers of ring opening on the Zr_{a1}-OH, Zr_{a2}-OH-Zr_b and Zr_{a2}-O_{3a2} sites. The O atoms of the OH groups participate actively by coordinating the C5 atom of THF. The ring opening on Zr_{a2}-OH-Zr_b is more facile than on the other two sites (free energy profiles and the corresponding analysis are provided in Section S3.1 in the Supplementary Materials). In the following, we consider catalytic pathways on Zr_{a2}-OH-Zr_b.

The salient elements of the dominant pathways are shown in Scheme 3 (detailed description in Section S3.2 in the Supplementary Materials). Pathway 1_Zrh to butadiene is similar to Pathway 1_Zrd (Scheme 2) on the dry-ZrO_2 surface. The minor differences between them lie in the type of the surface atoms participating in the proton-shuttling step. Specifically, on the hydroxylated surface, the atoms that participate in the reaction are Zr_{a2}, O_{3a2}, the bridging OH (O_b), and the terminal OH, whereas on the dry-ZrO_2 surface, the participating atoms are Zr_a, O_{3a}, and O_{3b} (Scheme 2). On Pathway 1_Zrh, after the γ-proton elimination step, a proton shuttles from the terminal OH to the bridging OH, whereas on the dry-ZrO_2 surface, the proton in $\mathbf{3_{Zrd}}$ shuttles from O_{3b} to O_{3a} ($TS6_{Zrd}$ in Section S3.2). More details are provided in Section S3.2. Regarding the retro-Prins reaction, Pathway 2_Zrh is the most dominant one and is mechanistically similar to Pathway 4_Zrd on the dry surface. In addition to the retro-Prins Pathway 2_Zrh, there is a less dominant one (Pathway 3_Zrh) described in Section S3.2.

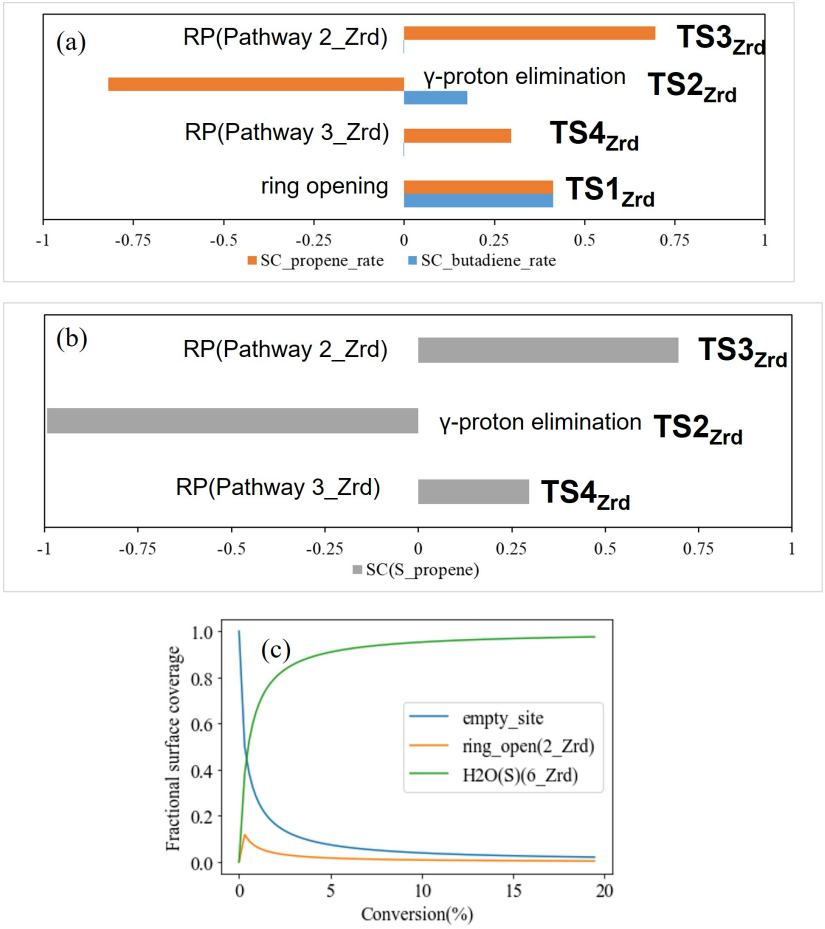

Figure 2. Microkinetic analysis of reaction on dry-ZrO_2: (**a**) sensitivity analysis for product formation rates; (**b**) sensitivity analysis for propene selectivity; (**c**) surface coverages in predominant species vs. conversion. (TS: Transition State; SC: Sensitivity coefficient; RP: Retro-Prins).

Comparing the free energy profiles for the dry and hydrous ZrO_2 surfaces (Figure S4a), we make two observations that have opposite effects on the THF dehydra-decyclization rate. First, the THF ring-opening barrier ($TS1_{Zrh}$ in Figure S4a) is 0.1 eV higher on the hydrous than on the dry surface, suggesting a slower reaction. Second, dissociated water ($\mathbf{6_{Zrh}}$) is less stable on the hydroxylated surface than on the dry one, which should result in a higher fraction of empty sites and hence higher reaction rates. Figure S4 shows the free energy and the enthalpy profiles of all four pathways. Similar to the dry-ZrO_2 model, enthalpy profiles show that THF, HCHO, and H_2O strongly chemisorb on the surface, with H_2O binding the strongest via dissociative chemisorption (Figure S4b).

To analyze these competing effects, we performed microkinetic modeling for the Zr_{a2}-O_{3a2} active site. The site density for Zr_{a2}-O_{3a2} is 4 sites/supercell, which is equal to the maximum number of Zr_{a2}-O_{3a2} sites in a 2 × 4 × 1 ZrO_2 supercell. We found that, although there is less surface water (**6_{Zrh}**) and more open sites on the hydrated surface (cf. Figures 2b and S5a), the turnover frequency (TOF) on the hydroxylated surface is 2.4 times as low as on the dry one (TOF values in Table S7). Thus, between the increase in the ring-opening barrier and the increase in the fraction of empty sites, the former has more of an impact on the TOF. $S_{butadiene}$ and $S_{propene}$ are 99.8% and 0.2%, respectively (Figure S5b), not much different from those on the dry surface and in good agreement with experiments [10]. Additionally, sensitivity analysis (Figure S5c,d) shows that, similar to the mechanism on the dry surface, the ring opening ($TS1_{Zrh}$) predominantly controls the reaction rates to butadiene and propene. While $S_{butadiene}$ is insensitive to the rate of any of the steps, $S_{propene}$ is enhanced by the retro-Prins step ($TS11_{Zrh}$) and hampered by the competing C-O bond cleavage step ($TS5_{Zrh}$).

Table 1 contains the apparent activation energies, E_a, obtained from the microkinetic analysis of the dry and hydroxylated ZrO_2 surface models. On account of the experimental E_a being closer to the hydroxylated than the dry zirconia model, one could reasonably infer that the former is a better representation of the real system. This prediction creates an avenue for experimentalists to perform spectroscopic experiments such as FTIR under operando conditions to identify the concentration and type of surface hydroxyl group and various other intermediates.

Table 1. Apparent activation energy values from experiment [10] and microkinetic simulations. The reactor parameters, reaction and feed conditions are shown in Table S8 in the Supplementary Materials.

Experiment/Model	E_a (kJ/mol)
Experiment	65.2 ± 12.1
Dry-ZrO_2	94.2 ± 0.3
Hydroxylated-ZrO_2	73.3 ± 0.2

3.3. Dry γ-Al_2O_3 (110)

We investigate the mechanism of THF conversion on both dry and hydroxylated surfaces of γ-Al_2O_3 (110). Although the Al_{III} site is hydroxylated at 400 °C [12,27,29–32], here we consider the dry surface as well in order to understand the effect of surface OH on the reaction mechanism.

THF coordinates to Al_{III} or Al_{IVb} sites with its oxygen and assumes an upright configuration (Figure 1c). The respective binding energies are −1.98 eV and −1.51 eV. Scheme 4 shows the salient features of the most dominant pathways that result from the binding of THF on the Al_{III} site (details in Section S4.1 in the Supplementary Materials). Pathway 1_Ald to butadiene is mechanistically similar to Pathway 1_Zrd, with some minor differences: first, and unlike Pathway 1_Zrd, on Pathway 1_Ald, the γ-proton elimination is not followed by proton hopping; and second, following butadiene desorption, the H_2O recombination is preceded by proton hopping. Pathway 2_Ald is the most dominant pathway to retro-Prins products and is mechanistically similar to Pathway 2_Zrd on dry-ZrO_2. There are two more retro-Prins pathways (Pathways 3_Ald and 4_Ald) described in Section S4.1, but they are associated with very low reaction fluxes and thereby are of minor catalytic interest. The free energy and enthalpy profiles of all the pathways are shown in Figure S6 in the Supplementary Materials. As seen in the cases of ZrO_2 models, enthalpy profiles (Figure S6b) show that both THF and HCHO chemisorb on the Al_{III} sites of the surface (ΔH_{ads_THF} = −2 eV and ΔH_{ads_HCHO} = −1.43 eV). H_2O can chemisorb on the surface both in undissociated (7_{Ald}) and dissociated forms (6_{Ald} and $5b_{Ald}$). When compared to ZrO_2 models, the binding strength of THF, HCHO, and dissociated H_2O are much higher on the dry-Al_2O_3 surface, and the strong binding of dissociated H_2O is also reflected in the highest free energy-based stability of intermediates 6_{Ald} and $5b_{Ald}$.

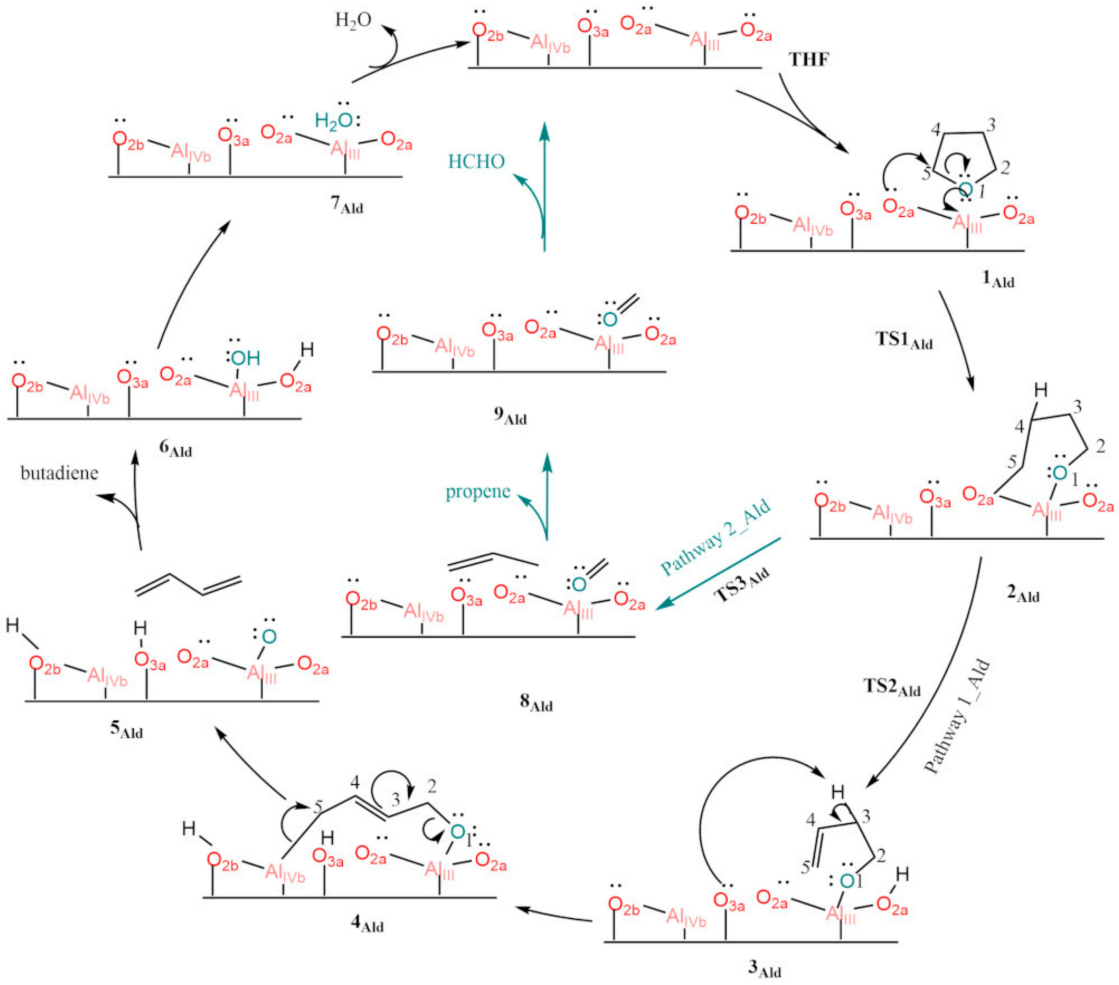

Scheme 4. Mechanism of THF reaction to butadiene and retro-Prins products on dry γ-Al_2O_3 (110). Pathway 1_Ald (in black): butadiene; Pathway 2_Ald (green): retro-Prins products. ('Ald' stands for dry-Al_2O_3).

Microkinetic analysis of fluxes of pathways (Table S9) and product selectivities (Figure 3a) confirm that Pathway 1_Ald has nearly 100% flux and hence, $S_{butadiene}$ is close to 100%, which does not agree with the experimental selectivity on Al_2O_3 [10]. Surface coverage analysis (Figure 3b) shows that at very low conversions (1%), the total fraction of chemisorbed H_2O is close to 1 (Figure 3b), a consequence of the hydrophilic nature of the Al_{III} site. This implies that once all the Al_{III} sites are blocked by chemisorbed H_2O, the surface becomes inactive. We also performed sensitivity analysis (Figure S7 in the Supplementary Materials) and the results were very similar to those on the dry t-ZrO_2 (101) surface. Considering the significant blocking of Al_{III} sites by water, we next turned our attention to the catalytic behavior of hydroxylated alumina.

3.4. Hydroxylated γ-Al_2O_3 (110)

The hydroxylated Al_2O_3 model (Figure 1d) consisted of a chemisorbed H_2O water molecule on the Al_{III}-O_{2a} site pair. Out of the three available sites, namely Al_{IVb}, Al_{IVa1}, and Al_{IVa2}, THF binds the strongest on Al_{IVb} (the respective binding energies are −1.86, −1.3, and −1.11 eV). The THF ring opening is more favorable on Al_{IVb}-O_{3b} than on Al_{IVb}-O_{2b} or Al_{IVb}-$OH_{terminal}$ (Figure S8). Hence, we investigated the reaction on the Al_{IVb}-O_{3b} site.

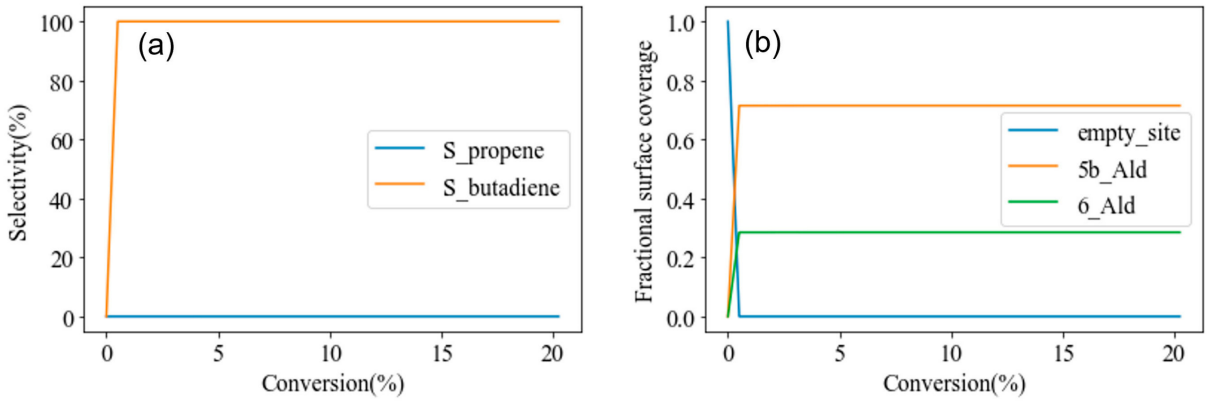

Figure 3. Microkinetic analysis of the dry-Al_2O_3 model. (**a**) Selectivity for butadiene and propene as a function of conversion. (**b**) Surface coverage in predominant species as a function conversion.

Scheme 5 shows the important features of the most dominant pathways for butadiene (Pathway 1_Alh) and retro-Prins (Pathway 2_Alh) (details in Section S5 in the Supplementary Materials). Pathway 1_Alh presents some significant differences from the pathways on ZrO_2 (dry and hydrous) and on dry Al_2O_3 described so far. First, after the ring opening, it is more favorable for the γ-proton to be abstracted from the distal surface oxygen O_{3b} (the O-site coordinating the C5 carbon of $\mathbf{2_{Alh}}$) than from the neighboring O_{3a2}; on ZrO_2 (dry and hydrous) and dry Al_2O_3, the γ-proton is abstracted by a neighboring surface O-site. The distal O_{3b} is involved because when Al_{III}-O_{2a} is hydroxylated, Al_{IVb}-O_{3b} is the most favorable site pair to bind the butenoxide-H^+ pair (see Table S10), and a similar observation is also found in the case of CH_4 dissociation to CH_3—H^+, where Al_{IVb}-O_{3b} is the most favorable site pair [31]. Second, unlike ZrO_2 and dry Al_2O_3, on the hydroxylated Al_2O_3 surface the butenoxide intermediate ($\mathbf{3_{Alh}}$) undergoes E2 elimination instead of E1cB elimination due to the absence of a vicinal undercoordinated Lewis-acidic metal site that would stabilize the excess charge on the resulting carbanion (vide infra). The E2 elimination in $\mathbf{3_{Alh}}$ entails simultaneous C-O bond cleavage and β-proton elimination to form $\mathbf{4_{Alh}}$ (physisorbed butadiene and chemisorbed H_2O). Pathway 2_Alh is the dominant retro-Prins pathway. The free energy profiles of pathways 1_Alh and 2_Alh are shown in Figure 4. There are two additional less important retro-Prins pathways (Pathways 3_Alh and 4_Alh) whose mechanisms and energy profiles are shown in Section S5. Some additional minor differences between Pathway 1_Alh and butadiene formation pathways on the other surfaces are also discussed in Section S5. Figure S9 shows the free energy and enthalpy profiles of all the four pathways. Similar to the dry Al_2O_3 model, THF and HCHO strongly chemisorb on the surface, and H_2O chemisorbs in both undissociated and dissociated forms. Additionally, the binding strengths of THF, HCHO, and dissociated H_2O species are higher than those on ZrO_2 models and lower than those on dry Al_2O_3.

Unlike the reaction free energy profiles on ZrO_2 (dry and hydrous) and dry Al_2O_3, where the ring opening presents the higher transition state (cf. Figures S1, S4 and S6), it is the γ-proton elimination that presents the higher transition state ($TS3_{Alh}$) on hydrous ZrO_2, suggesting a change in the rate-determining step. These observations are confirmed by microkinetic analysis, presented next.

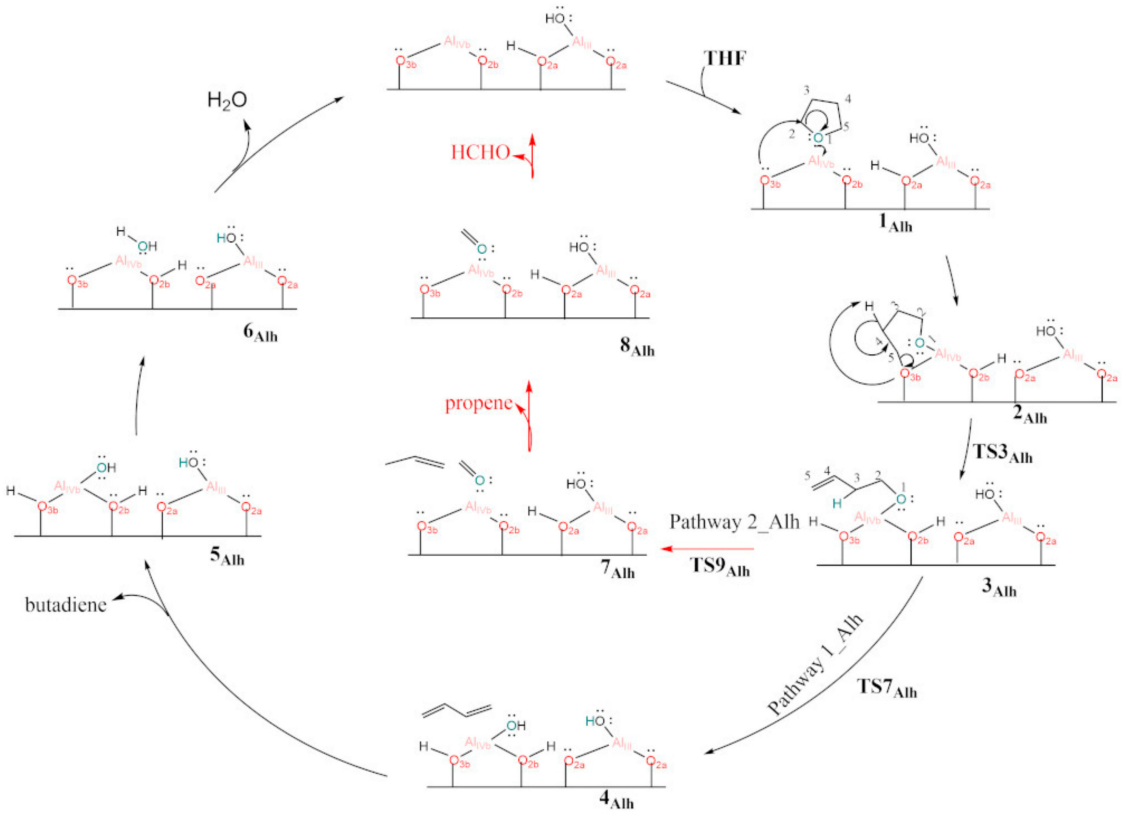

Scheme 5. Mechanism of THF reaction on Al_{IVb} site of hydroxylated γ-Al_2O_3 (110). Pathway 1_Alh (in black): butadiene; Pathway 2_Alh (red): retro-Prins products. ('Alh' stands for hydroxylated Al_2O_3).

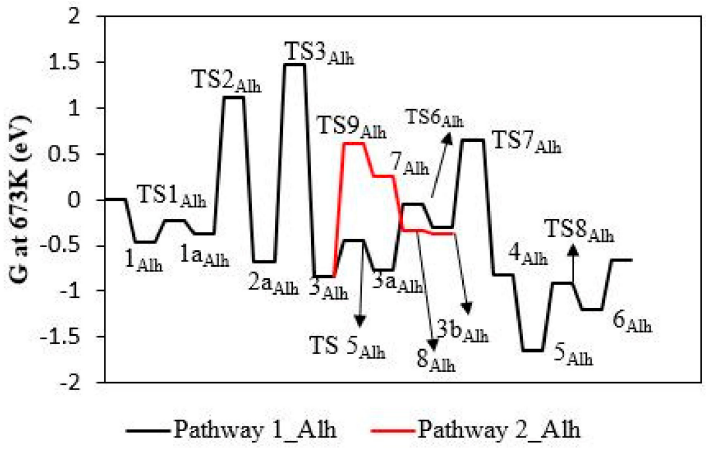

Figure 4. Free energy profile corresponding to Scheme 5 at 673.15 K.

The microkinetic analysis of reaction fluxes (Table S11) further confirms that Pathway 2_Alh is the most favorable pathway; the flux percentages through pathways 1_Alh, 2_Alh, and 3_Alh are 28%, 51.4%, and 20% respectively. At low conversions, propene is more selective than butadiene (Figure 5a), which is in qualitative agreement with the experimental selectivity on Al_2O_3 [10]. As the conversion increases, thermodynamics takes over and the selectivity for butadiene gradually increases. At ~15% conversion, the selectivities for butadiene and propene are the same. At conversion close to the equilibrium value at 673 K (99.96%), $S_{butadiene}$ and $S_{propene}$ approach their respective equilibrium values of 91.1% and 8.9%, respectively (Section S6 of Supplementary Materials). Surface coverage analysis (Figure 5b) shows that at low conversions, the ring opened intermediate (**2_{Alh}**) is

the most abundant one due to the slowest rate of γ-proton elimination. As the conversion increases, $S_{butadiene}$ and the fraction of chemisorbed H_2O (**5$_{Alh}$**) increase.

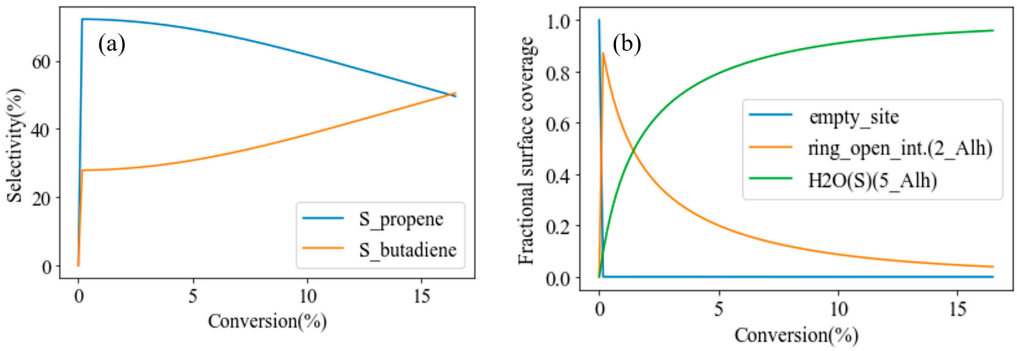

Figure 5. Microkinetic analysis corresponding to the hydroxylated Al_2O_3 model: (**a**) selectivity of butadiene and propene vs. conversion, and (**b**) surface coverages in predominant species vs. conversion.

Sensitivity analysis (Figure 6a) further confirms that the γ-proton elimination ($TS3_{Alh}$) is rate-limiting for both butadiene and propene formation, as suggested by the free energy profiles. The slowest rate for γ-proton elimination is likely to be responsible for the high surface coverage of ring-opened intermediate (**2$_{Alh}$**) at low conversions (Figure 6b). Here, we should recall that when we compared the ring opening barriers on Al_{IVb}-O_{3b}, Al_{IVb}-$OH_{terminal}$, and Al_{IVb}-O_{2b} sites (to select the most favorable pathway for the mechanistic investigation (Figure S8)) we assumed that ring opening is the RDS. Since the γ-proton elimination was found to be the RDS, we revisit the comparison made in Figure S8 to make sure that the choice of the Al_{IVb}-O_{3b} site for the mechanistic investigation is still meaningful. In Figure S11, we compare the energy of $TS3_{Alh}$ with the TS energies of ring opening on Al_{IVb}-$OH_{terminal}$ and Al_{IVb}-O_{2b} (TS_{OH} and TS_{O2b}, respectively). Figure S11 confirms that the choice of Al_{IVb}-O_{3b} site for mechanistic investigation is meaningful since the energy of TS_{3Alh} is lower than the energies of TS_{OH} and TS_{O2b}.

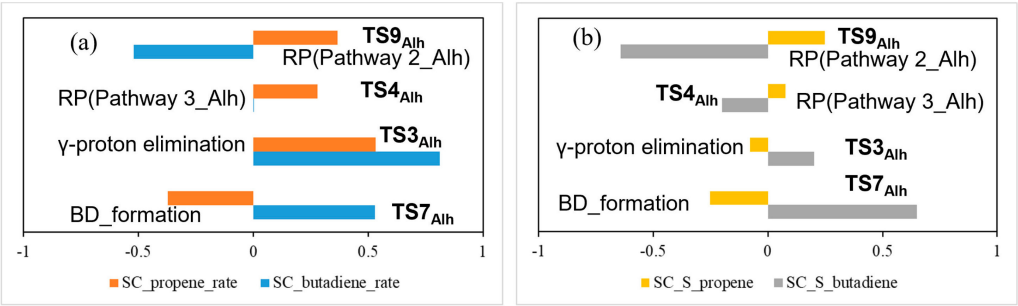

Figure 6. Microkinetic analysis corresponding to the hydroxylated Al_2O_3 model: (**a**) sensitivity analysis for rates of product formation; (**b**) sensitivity analysis for selectivity of product formation. (TS: Transition State; SC = Sensitivity Coefficient; RP = Retro-Prins; BD = Butadiene.).

Returning to the sensitivity analysis, in addition to $TS3_{Alh}$, the rate of propene formation is enhanced by the retro-Prins steps on pathways 2_Alh ($TS9_{Alh}$) and 3_Alh ($TS4_{Alh}$, see Figure S9) and hampered by the E2 elimination step ($TS7_{Alh}$). Figure 6b shows that $S_{propene}$ is mainly enhanced and hampered by retro-Prins ($TS9_{Alh}$) and E2 elimination steps ($TS7_{Alh}$), respectively. In contrast, the rate and selectivity of butadiene formation are mainly enhanced and hampered by E2 elimination ($TS7_{Alh}$) and retro-Prins steps ($TS9_{Alh}$), respectively.

4. Discussion

Based on the results obtained so far, we observe that the difference in product selectivities between hydroxylated Al_2O_3 and the rest of the surfaces can mainly be attributed to the difference in the free energy barriers of the retro-Prins and dehydration/elimination

steps that branch off at the butenoxide intermediate. Therefore, analyzing the variations in energy barriers of these specific dehydration and retro-Prins steps will help us explain the surface-dependent product selectivity.

On the surfaces (dry Al_2O_3, dry and hydroxylated ZrO_2) that favor the formation of butadiene, the dehydration of the butenoxide intermediate is E1cB, whereas on hydroxylated Al_2O_3, the dehydration is E2. In E1cB, the β-proton of the butenoxide intermediate is abstracted by a basic O-site on the surface and the corresponding carbanion is stabilized by the surface metal site (intermediates $\mathbf{4_{Zrd}}$, $\mathbf{4_{Zrh}}$, and $\mathbf{4_{Ald}}$ in Schemes 2–4 respectively); the position of the double bond shifts from C4-C5 to C3-C4, and the C5 carbon forms a bond with the surface metal site. This surface-stabilized intermediate further undergoes facile C-O bond cleavage (intrinsic barrier in the range of 0.3–0.6 eV) to butadiene and chemisorbed H_2O. However, on hydroxylated Al_2O_3, there is no proximal undercoordinated metal site to stabilize the E1cB intermediate, hence the elimination is E2—the β-C-H and C-O bonds are broken simultaneously. The free energy barriers for E1cB are in the range of 1–1.2 eV and lower than the E2 free energy barrier on hydroxylated Al_2O_3 (1.5 eV).

We believe that the E1cB barriers are lower than the E2 barriers because the former transition states are stabilized by the interaction between the C5 carbon and a surface metal site, which is not the case in E2. In the E1cB transition state, the negative charge on C3 delocalizes over the allylic C4-C5 double bond while the charge on C5 is stabilized by the proximal Lewis-acidic metal site. E2 is favored on hydroxylated Al_2O_3 because there is not a proximal surface metal site that could interact with the C5 atom. Charge density difference (CDD) and electron localization function (ELF) analyses indicate an ionic interaction between C5 and a proximal Lewis-acidic metal site, as discussed in Section S7 in the Supplementary Materials.

Despite the absence of a neighboring Lewis-acidic metal site on hydroxylated Al_2O_3, we tested the β-proton elimination of the E1cB mechanism by stabilizing the resulting carbanion on a surface proton (which originated from the γ-proton elimination) (Figure S12a). The barrier for this step is very high compared to the barrier for the E2 step (Figure S12b), implying that the TS of the β-proton elimination is likely to be charge stabilized only by a Lewis-acidic metal site and not by any other electrophilic site.

Regarding the retro-Prins products, the intrinsic barriers for propene formation from the butenoxide intermediate vary across the investigated surfaces which can be ranked as follows: hydroxylated Al_2O_3 < hydroxylated ZrO_2 < dry ZrO_2 < dry Al_2O_3. It is not straightforward to rationalize the differences in these energy barriers because the retro-Prins step from the butenoxide intermediate is a concerted mechanism and involves multiple chemical and geometric factors: C2-C3 bond cleavage, C5-H bond formation, $O_{surface}$-H bond cleavage, O1-M bond cleavage, C2=O1 bond formation, the dihedral angle between H, C5, C3, and C2, etc. By merely using the limited data we have in this study, it is challenging to relate those factors to the energy of the retro-Prins TS.

Therefore, a higher barrier for butadiene formation, due to the lack of a proximal Lewis-acid metal site, and a relatively lower barrier for retro-Prins reaction make hydroxylated Al_2O_3 more selective towards propene at low conversions. The local topology around the active site plays a crucial role in determining the product selectivities by deciding the dominant reaction channel.

5. Conclusions

We have used density functional theory (DFT) and microkinetic modeling to understand the differences in selectivity for products obtained from the dehydra-decyclization of THF on ZrO_2 and Al_2O_3. We use t-ZrO_2 (101) and γ-Al_2O_3 (110) models to investigate the reaction mechanism and investigate the effect of H_2O on the reaction mechanism.

On the dry surface of t-ZrO_2 (101), the selectivity of butadiene is close to 100% which is in good agreement with the experiment. Ring opening is the rate-determining step, and the retro-Prins products are predominantly formed by a concerted C-C bond cleavage and hydride shift of the ring opened intermediate. Chemisorbed H_2O is the most abundant

surface species. The OH-groups on the hydroxylated ZrO_2 surface neither enhance the reaction rate nor significantly affect the product selectivity. Despite insignificant differences in the rates and product selectivities between dry and hydroxylated ZrO_2, the pathway that predominantly contributes to the formation of propene is different on both surfaces; when surface OH-groups are involved, propene is predominantly formed from the butenoxide intermediate ($\mathbf{3_{Zrh}}$).

The reaction behavior on hydroxylated Al_2O_3 differs greatly from the other investigated surfaces. At low conversions, the retro-Prins products are predominantly produced from the butenoxide intermediate ($\mathbf{3_{Alh}}$) at 70% selectivity, which is in qualitative agreement with the experiments. Beyond 15% conversion, thermodynamics overtakes kinetics and the catalyst becomes more selective for butadiene. Moreover, on hydroxylated Al_2O_3, the γ-proton elimination is the rate-determining step.

The main difference in product selectivities between hydroxylated Al_2O_3 and the ZrO_2 (dry and hydrous) lies in the barriers for retro-Prins and elimination reactions of the butenoxide intermediate. On hydroxylated Al_2O_3 and ZrO_2, the butenoxide intermediate undergoes E2 and E1cB reactions, respectively. The presence of a neighboring Lewis-acidic metal site facilitates the E1cB mechanism, which is more facile than an E2, which is preferred when such Lewis acid centers are not available. We believe that the interaction between the terminal carbon (C5) and the surface Lewis-acidic metal site in the E1cB transition state makes this step more facile than E2, where the C5-metal interaction is lacking. The local topology around the reacting site surely greatly influences the reaction mechanism and thereby the selectivity.

Supplementary Materials: The following supporting information can be downloaded at: https://www.mdpi.com/article/10.3390/chemistry5010031/s1 The Supplementary Materials contain a word document (SI) that contains information about microkinetic input parameters, additional microkinetic results, derivations, and free energy profiles. The material also contains an Excel file (energies and vibrational frequencies.xlsx) that contains energies and vibrational frequencies of gaseous species, intermediates, and transition states. The supplementary material also contains coordinates of all the structures and transition states along with other DFT input files, and input files of microkinetic modelling. The complete set of DFT files are available in the Zenodo database (https://doi.org/10.5281/zenodo.7686469, accessed on 31 January 2023)

Author Contributions: Conceptualization, S.P.B., S.C. and D.G.V.; methodology, S.P.B. and S.C.; software, S.P.B.; validation, S.P.B., S.C. and D.G.V.; formal analysis, S.P.B.; investigation, S.P.B.; resources, D.G.V.; data curation, S.P.B.; writing—original draft preparation, S.P.B. and S.C.; writing—review and editing, S.P.B., S.C. and D.G.V.; visualization, S.P.B.; supervision, S.C. and D.G.V.; project administration, S.C. and D.G.V.; funding acquisition, S.C. and D.G.V. All authors have read and agreed to the published version of the manuscript.

Funding: This work was supported by the Catalysis Center for Energy Innovation (CCEI), an Energy Frontier Research Center funded by the U. S. Department of Energy, Office of Science, Office of Basic Energy Sciences, under Award number DE-SC0001004.

Data Availability Statement: Data are contained within the article and Supplementary Material.

Acknowledgments: This research was supported in part through the use of Information Technologies (IT) resources at the University of Delaware, specifically the high-performance computing resources. We also thank Raymond Gorte, Omar Abdelrahman and their respective research groups for providing experimental insights. We also thank Gerhard Wittreich for providing his valuable insights. We dedicate this paper to our friend Avelino Corma for his enormous contributions to the catalysis field.

Conflicts of Interest: The authors declare no conflict of interest.

References

1. Choudhary, V.; Pinar, A.B.; Sandler, S.I.; Vlachos, D.G.; Lobo, R.F. Xylose Isomerization to Xylulose and Its Dehydration to Furfural in Aqueous Media. *ACS Catal.* **2011**, *1*, 1724–1728. [CrossRef]
2. Choudhary, V.; Sandler, S.I.; Vlachos, D.G. Conversion of Xylose to Furfural Using Lewis and Brønsted Acid Catalysts in Aqueous Media. *ACS Catal.* **2012**, *2*, 2022–2028. [CrossRef]
3. Wang, S.; Vorotnikov, V.; Vlachos, D.G. Coverage-Induced Conformational Effects on Activity and Selectivity: Hydrogenation and Decarbonylation of Furfural on Pd(111). *ACS Catal.* **2015**, *5*, 104–112. [CrossRef]
4. Li, X.; Jia, P.; Wang, T. Furfural: A Promising Platform Compound for Sustainable Production of C4 and C5 Chemicals. *ACS Catal.* **2016**, *6*, 7621–7640. [CrossRef]
5. Abdelrahman, O.A.; Park, D.S.; Vinter, K.P.; Spanjers, C.S.; Ren, L.; Cho, H.J.; Vlachos, D.G.; Fan, W.; Tsapatsis, M.; Dauenhauer, P.J. Biomass-Derived Butadiene by Dehydra-Decyclization of Tetrahydrofuran. *ACS Sustain. Chem. Eng.* **2017**, *5*, 3732–3736. [CrossRef]
6. Kumbhalkar, M.D.; Buchanan, J.S.; Huber, G.W.; Dumesic, J.A. Ring Opening of Biomass-Derived Cyclic Ethers to Dienes over Silica/Alumina. *ACS Catal.* **2017**, *7*, 5248–5256. [CrossRef]
7. Kumar, G.; Liu, D.; Xu, D.; Ren, L.; Tsapatsis, M.; Dauenhauer, P.J. Dehydra-Decyclization of 2-Methyltetrahydrofuran to Pentadienes on Boron-Containing Zeolites. *Green Chem.* **2020**, *22*, 4147–4160. [CrossRef]
8. Li, S.; Abdelrahman, O.A.; Kumar, G.; Tsapatsis, M.; Vlachos, D.G.; Caratzoulas, S.; Dauenhauer, P.J. Dehydra-Decyclization of Tetrahydrofuran on H-ZSM5: Mechanisms, Pathways, and Transition State Entropy. *ACS Catal.* **2019**, *9*, 10279–10293. [CrossRef]
9. Wang, C.; Li, S.; Mao, X.; Caratzoulas, S.; Gorte, R.J. H-D Exchange of Simple Aromatics as a Measure of Brønsted-Acid Site Strengths in Solids. *Catal. Lett.* **2018**, *148*, 3548–3556. [CrossRef]
10. Ji, Y.; Lawal, A.; Nyholm, A.; Gorte, R.J.; Abdelrahman, O.A. Dehydra-Decyclization of Tetrahydrofurans to Diene Monomers over Metal Oxides. *Catal. Sci. Technol.* **2020**, *10*, 5903–5912. [CrossRef]
11. Ji, Y.; Batchu, S.P.; Lawal, A.; Vlachos, D.G.; Gorte, R.J.; Caratzoulas, S.; Abdelrahman, O.A. Selective Dehydra-Decyclization of Cyclic Ethers to Conjugated Dienes over Zirconia. *J. Catal.* **2022**, *410*, 10–21. [CrossRef]
12. Digne, M.; Sautet, P.; Raybaud, P.; Euzen, P.; Toulhoat, H. Hydroxyl Groups on γ-Alumina Surfaces: A DFT Study. *J. Catal.* **2002**, *211*, 1–5. [CrossRef]
13. Christensen, A.; Carter, E.A. First-principles study of the surfaces of zirconia. *Phys. Rev. B* **1998**, *58*, 1–15. [CrossRef]
14. Hofmann, A.; Clark, S.J.; Oppel, M.; Hahndorf, I. Hydrogen Adsorption on the Tetragonal ZrO_2(101) Surface: A Theoretical Study of an Important Catalytic Reactanty. *Phys. Chem. Chem. Phys.* **2002**, *4*, 3500–3508. [CrossRef]
15. Yang, Y.; Lin, F.; Tran, H.; Chin, Y.H.C. Butanal Condensation Chemistry Catalyzed by Brønsted Acid Sites on Polyoxometalate Clusters. *ChemCatChem* **2017**, *9*, 287–299. [CrossRef]
16. Lin, F.; Yang, Y.; Chin, Y.H. Kinetic Requirements of Aldehyde Transfer Hydrogenation Catalyzed by Microporous Solid Brønsted Acid Catalysts. *ACS Catal.* **2017**, *7*, 6909–6914. [CrossRef]
17. Blochl, P.E.; Forst, C.J.; Schimpl, J. Projector Augmented Wave Method: Ab Initio Molecular Dynamics with Full Wave Functions. *Bull. Mater. Sci.* **2003**, *26*, 33–41. [CrossRef]
18. Ernzerhof, M.; Scuseria, G.E. Assessment of the Perdew–Burke–Ernzerhof Exchange-Correlation Functional. *J. Chem. Phys.* **1999**, *110*, 5029–5036. [CrossRef]
19. Becke, A.D.; Johnson, E.R. A Density-Functional Model of the Dispersion Interaction. *J. Chem. Phys.* **2005**, *123*, 154101. [CrossRef]
20. Henkelman, G.; Jónsson, H. A Dimer Method for Finding Saddle Points on High Dimensional Potential Surfaces Using Only First Derivatives. *J. Chem. Phys.* **1999**, *111*, 7010–7022. [CrossRef]
21. Henkelman, G.; Uberuaga, B.P.; Jónsson, H. Climbing Image Nudged Elastic Band Method for Finding Saddle Points and Minimum Energy Paths. *J. Chem. Phys.* **2000**, *113*, 9901–9904. [CrossRef]
22. Grimme, S. Supramolecular Binding Thermodynamics by Dispersion-Corrected Density Functional Theory. *Chem. A Eur. J.* **2012**, *18*, 9955–9964. [CrossRef] [PubMed]
23. Li, Y.P.; Gomes, J.; Sharada, S.M.; Bell, A.T.; Head-Gordon, M. Improved Force-Field Parameters for QM/MM Simulations of the Energies of Adsorption for Molecules in Zeolites and a Free Rotor Correction to the Rigid Rotor Harmonic Oscillator Model for Adsorption Enthalpies. *J. Phys. Chem. C* **2015**, *119*, 1840–1850. [CrossRef]
24. Schoonheydt, R.A.; Weckhuysen, B.M. Editorial Highlight: Molecules in Confined Spaces. *Phys. Chem. Chem. Phys.* **2009**, *11*, 2794–2798. [CrossRef] [PubMed]
25. Lym, J.; Wittreich, G.R.; Vlachos, D.G. A Python Multiscale Thermochemistry Toolbox (PMuTT) for Thermochemical and Kinetic Parameter Estimation. *Comput. Phys. Commun.* **2020**, *247*, 106864. [CrossRef]
26. Chen, H.Y.T.; Tosoni, S.; Pacchioni, G. Adsorption of Ruthenium Atoms and Clusters on Anatase TiO2 and Tetragonal ZrO_2(101) Surfaces: A Comparative DFT Study. *J. Phys. Chem. C* **2015**, *119*, 10856–10868. [CrossRef]
27. Digne, M.; Sautet, P.; Raybaud, P.; Euzen, P.; Toulhoat, H. Use of DFT to Achieve a Rational Understanding of Acid-Basic Properties of γ-Alumina Surfaces. *J. Catal.* **2004**, *226*, 54–68. [CrossRef]
28. Coltrin, M.E.; Kee, R.J.; Rupley, F.M. Surface Chemkin: A General Formalism and Software for Analyzing Heterogeneous Chemical Kinetics at a Gas-surface Interface. *Int. J. Chem. Kinet.* **1991**, *23*, 1111–1128. [CrossRef]
29. Valero, M.C.; Digne, M.; Sautet, P.; Raybaud, P. DFT Study of the Interaction of a Single Palladium Atom with γ -Alumina Surfaces: The Role of Hydroxylation. *Oil Gas Sci. Technol.-Rev. l'IFP* **2006**, *61*, 535–545. [CrossRef]

30. Wischert, R.; Copéret, C.; Delbecq, F.; Sautet, P. Optimal Water Coverage on Alumina: A Key to Generate Lewis Acid-Base Pairs That Are Reactive towards the C-H Bond Activation of Methane. *Angew. Chem. Int. Ed.* **2011**, *50*, 3202–3205. [CrossRef]
31. Wischert, R.; Laurent, P.; Copéret, C.; Delbecq, F.; Sautet, P. γ-Alumina: The Essential and Unexpected Role of Water for the Structure, Stability, and Reactivity of "Defect" Sites. *J. Am. Chem. Soc.* **2012**, *134*, 14430–14449. [CrossRef] [PubMed]
32. Batchu, S.P.; Wang, H.-L.; Chen, W.; Zheng, W.; Caratzoulas, S.; Lobo, R.F.; Vlachos, D.G. Ethane Dehydrogenation on Single and Dual Centers of Ga-Modified γ-Al_2O_3. *ACS Catal.* **2021**, *11*, 1380–1391. [CrossRef]

Disclaimer/Publisher's Note: The statements, opinions and data contained in all publications are solely those of the individual author(s) and contributor(s) and not of MDPI and/or the editor(s). MDPI and/or the editor(s) disclaim responsibility for any injury to people or property resulting from any ideas, methods, instructions or products referred to in the content.